

Validation of Pore-Scale Simulations of Hydrodynamic Dispersion in Random Sphere Packings

Siarhei Khirevich, Alexandra Hörtzel and Ulrich Tallarek*

Department of Chemistry, Philipps-Universität Marburg, Hans-Meerwein-Strasse, 35032 Marburg, Germany.

Received 31 October 2011; Accepted (in revised version) 26 January 2012

Available online 29 August 2012

Abstract. We employ the lattice Boltzmann method and random walk particle tracking to simulate the time evolution of hydrodynamic dispersion in bulk, random, mono-disperse, hard-sphere packings with bed porosities (interparticle void volume fractions) between the random-close and the random-loose packing limit. Using Jodrey-Tory and Monte Carlo-based algorithms and a systematic variation of the packing protocols we generate a portfolio of packings, whose microstructures differ in their degree of heterogeneity (DoH). Because the DoH quantifies the heterogeneity of the void space distribution in a packing, the asymptotic longitudinal dispersion coefficient calculated for the packings increases with the packings' DoH. We investigate the influence of packing length (up to $150 d_p$, where d_p is the sphere diameter) and grid resolution (up to 90 nodes per d_p) on the simulated hydrodynamic dispersion coefficient, and demonstrate that the chosen packing dimensions of $10 d_p \times 10 d_p \times 70 d_p$ and the employed grid resolution of 60 nodes per d_p are sufficient to observe asymptotic behavior of the dispersion coefficient and to minimize finite size effects. Asymptotic values of the dispersion coefficients calculated for the generated packings are compared with simulated as well as experimental data from the literature and yield good to excellent agreement.

PACS: 47.56.+r, 81.05.Rm, 05.40.-a, 61.43.Bn, 02.60.Cb

Key words: Packing microstructure, degree of heterogeneity, packing algorithm, hydrodynamic dispersion, random sphere packings.

1 Introduction

Mass transport in porous media is a central research theme in science and engineering, affecting such diverse fields as, e.g., separation of chemicals by chromatography, catalytic

*Corresponding author. *Email addresses:* khirevic@staff.uni-marburg.de (S. Khirevich), hoeltzel@staff.uni-marburg.de (A. Hörtzel), tallarek@staff.uni-marburg.de (U. Tallarek)

reactions using fixed-bed adsorbents, migration of soil pollutants, and water recovery. Deriving morphology-transport relations to predict the transport properties of a porous medium from its pore space structure is therefore of fundamental as well as applied interest [1, 2]. The central structure-transport relationships can be established based on experimental data from high-resolution techniques that enable the physical reconstruction of a porous medium, such as X-ray tomography [3–5], nuclear magnetic resonance imaging [6], and confocal laser scanning microscopy [7, 8]. A real porous medium is the result of its formation process and has definite properties that cannot be altered at will by the researcher. Contrariwise, computer-generated models of porous media, such as random sphere packings (particulate fixed beds, in general), allow the systematic variation of packing properties (e.g., the final bed density, the particle porosity, as well as particle shape and size distribution functions) independent of other parameters. Random sphere packings, for example, can be computer-generated with high reproducibility over a range of bed porosities (interparticle void volume fractions), which is a pre-requisite to study the porosity-scaling of the transport coefficients for hydraulic permeability, effective diffusion, and hydrodynamic dispersion [9–11]. Another consideration is the observation of asymptotic behavior of the mass transport coefficients in the simulations, which requires packing models of sufficient size. As of now, samples that fit this requirement are difficult to obtain by physical reconstruction, whereas large computer-generated packings are readily available. The benefit of performing hydrodynamic dispersion simulations up to the asymptotic limit lies in the unequivocal meaning of the time-independent values of the transport coefficients. Only asymptotic values can be compared with certainty, which is of particular importance when packings with systematically varied DoH are studied, and asymptotic values for the mass transport coefficients are also needed to fit equations that link specific structural features of a porous medium to its (effective) mass transport properties [12].

The complex solid-liquid boundaries characterizing the pore space of a porous medium (whether a reconstructed sample or a computer-generated model) and the large model size required to observe asymptotic behavior of the mass transport coefficients needs supercomputing resources to perform pore-scale simulations of advective-diffusive transport. In this work, we perform pore-scale simulations of hydrodynamic dispersion in bulk (unconfined) random packings of uniform, hard spheres. These packings mimic infinitely wide, randomly packed beds without walls, and our simulations therefore selectively address bulk transport properties. A set of packings with targeted bed properties (final packing density, systematically varied DoH) are generated with two principally different algorithms, and fluid flow and advective-diffusive mass transport inside the packings' void space is simulated by the lattice Boltzmann (LBM) and random-walk particle-tracking (RWPT) methods, respectively. LBM and RWPT are attractive for use on supercomputers, because their local update rule minimizes the information transfer (communication time) between the processing units during execution of a parallel program, leaving the maximum amount of computation time for the calculations.

In this work we are interested in quantifying hydrodynamic dispersion resulting from

molecular diffusion and the inequalities of the local values of the linear velocity in the different channels available to the fluid stream in a packing. This process is critically affected by a packing's DoH, resulting in an intrinsic morphology-transport behavior and hydrodynamic dispersion. We describe our simulation workflow and discuss the chosen methods and algorithms with respect to large-scale simulations of hydrodynamic dispersion in random sphere packings. We quantify the influence of simulation parameters such as the boundary conditions, the grid resolution, and the packing length on the resulting numerical error, and validate our approach by comparison with literature data, both from experiments and numerical simulations.

2 Generation of random sphere packings

An unconfined random packing of uniform, monosized, hard spheres is fully described by the set of spatial coordinates of the sphere centers and the sphere diameter. Each packing has a distinct microstructure, i.e., a particular distribution of solid and void space within the packing. The packing microstructure is not captured by the packing's bed porosity ε , which gives only the void volume fraction. Instead, systematic microstructural differences between bulk random sphere packings are described by their degree of heterogeneity (DoH) [9, 13]. A packing's DoH can be understood as the amount of heterogeneity in the void space distribution and can be unequivocally determined by spatial tessellation and statistical analysis methods. The DoH of a packing determines its transport properties, which is why the study of structure-transport relationships in porous media requires a portfolio of random sphere packings with varying DoHs over a range of bed porosities [9, 10]. Equally important for mass transport simulations in porous media are the packing dimensions: simulation of hydrodynamic dispersion up to the asymptotic limit necessitates sufficiently large packings containing about 10^3 - 10^4 spheres. To generate sufficiently large packings with systematically varied DoH and bed porosity, we use either a modified Jodrey-Tory (JT) algorithm [14] or a Monte Carlo-based procedure [15].

A modified JT algorithm starts from a random distribution of N_{sp} sphere centers in a simulation box of volume V_{box} . Sphere overlap is typical in the initial configuration if the targeted (final) bed porosity ε_{fin} is low. The value of N_{sp} is calculated from ε_{fin} , V_{box} , and the final sphere diameter d_{fin} as

$$\varepsilon_{\text{fin}} = 1 - \frac{N_{\text{sp}} \pi d_{\text{fin}}^3}{6V_{\text{box}}}. \quad (2.1)$$

Each iteration includes i) the search of two sphere centers C_1 and C_2 with the minimum pair-wise distance d_{min} , where d_{min} defines the maximal sphere diameter at which no overlap occurs in the current packing configuration with the corresponding bed porosity

$$\varepsilon_{\text{min}} = 1 - \frac{N_{\text{sp}} \pi d_{\text{min}}^3}{6V_{\text{box}}}, \quad (2.2)$$

and ii) the symmetrical spreading of these two sphere centers along a line C_1C_2 up to a new distance, d_{\max} , according to the following equation:

$$d_{\max} = d_{\min} \left(1 + \alpha \log_{10} \left(\frac{d_{\text{fin}}}{d_{\min}} \right) \right), \quad (2.3)$$

where α is a constant. According to Eq. (2.3), as d_{\min} asymptotically approaches d_{fin} , ε_{\min} approaches ε_{fin} . The algorithm exits when the condition

$$|\varepsilon_{\min} - \varepsilon_{\text{fin}}| < 0.001 \varepsilon_{\text{fin}} \quad (2.4)$$

is satisfied. The functional dependence $d_{\max} = f(d_{\min})$ may be chosen differently, but each choice affects the convergence possibility and rate as well as the lower limit of bed porosities that can be realized.

The initial distribution of sphere centers and the value of the constant α , which according to Eq. (2.3) defines the magnitude for the displacement of sphere centers C_1 and C_2 , are varied to generate JT-packings with different DoHs. In this work, JT-packings are denoted as "TxA", where T is the type of initial distribution of sphere centers (R or S, see below) and A is the value of α . (For $\alpha = 1$, the generated packings are referred to as "T".) R-packings generation starts from a uniform random distribution of sphere centers in the simulation box, whereas for S-packings the simulation box was initially divided into N_{sp} equal cubic cells and each cell was then filled with one sphere center, placed in a random position into the cell. With a small value of α sphere centers tend to remain close to their initial positions during packing generation, so that the final packing configuration reflects the randomness of the initial distribution; a larger value of α provides a more homogeneous distribution of sphere centers in the final configuration.

The influence of the initial distribution scheme and the value of the parameter α on the final packing microstructure is demonstrated in Fig. 1, where the sphere packings are replaced by two-dimensional disk packings for clarity. The microstructure of the final packings in selected regions is compared with the respective initial disk distributions in Fig. 1. The generated packings reflect their respective packing protocols: i) S-packings are more homogeneous than R-packings, due to the more uniform initial disk distribution, and ii) initial maldistribution of void space is best balanced in the Sx6 configuration and least balanced in the Rx0.001 configuration.

Monte Carlo (MC)-based packing generation starts from a uniform distribution of N_{sp} spheres of diameter d_p in a dilute cubic array derived from expansion of a simple cubic packing by a factor F while keeping the sphere diameter constant. In our simulations we use $F = 2$ resulting in an 8 times larger volume of the initial packing domain compared with a packing where N_{sp} spheres are arranged in a simple cubic array. Then each sphere is moved in a random direction a distance Δd . If a given sphere intersects with another, the move is rejected. The distance Δd depends on the current fraction of accepted moves a : Δd is decreased when $a < 0.5$ and vice versa. After a series of N_{it} iterations is performed for the whole sphere ensemble ($N_{\text{it}} = 5000$ in this work), the minimal distance

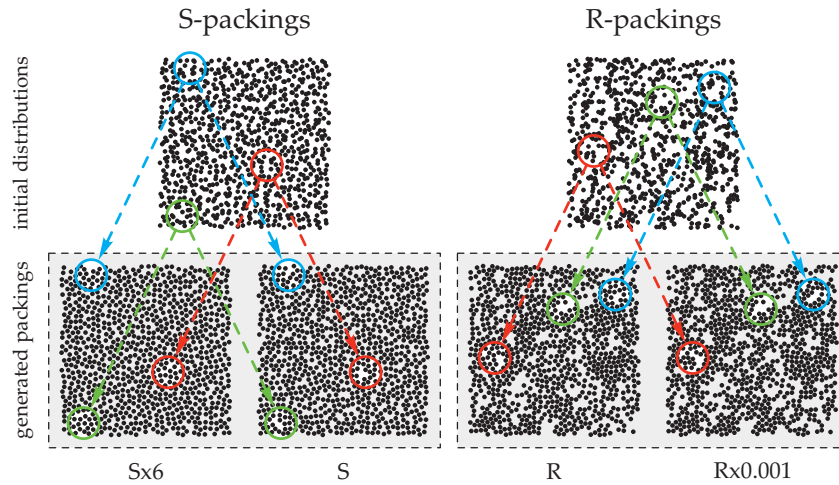


Figure 1: Bulk random packings of 900 monosized hard disks at $\epsilon \approx 0.46$ generated with the JT algorithm using different packing protocols. Shown are the initial distributions of the disks for S- and R-configurations (top) and the generated two-dimensional packings ((Sx6, S) and (R, Rx0.001); bottom). Circles around selected regions help to compare initial and final disk distribution in the packings.

between sphere centers d_{\min} is calculated and the simulation box is scaled by the factor $d_p / [d_p + \Omega \cdot (d_{\min} - d_p)]$ while keeping the sphere diameter constant. Here, Ω is the compression rate $0 < \Omega \leq 1$. By compression, the bed porosity decreases and the algorithm stops execution when the current porosity reaches the targeted value ϵ_{fin} . MC-packings are denoted as “ $\Omega \times C$ ” where C is the magnitude of the compression rate Ω used in the packing protocol.

MC-based methods tend to create closely-packed (quasi-crystalline) regions within a packing when slow compression rates and low packing densities are combined, as mentioned in [16]. We demonstrate this with two-dimensional disk packings. Packings generated with slower and faster compression rates ($\Omega = 0.025$ and 0.99 , respectively) are

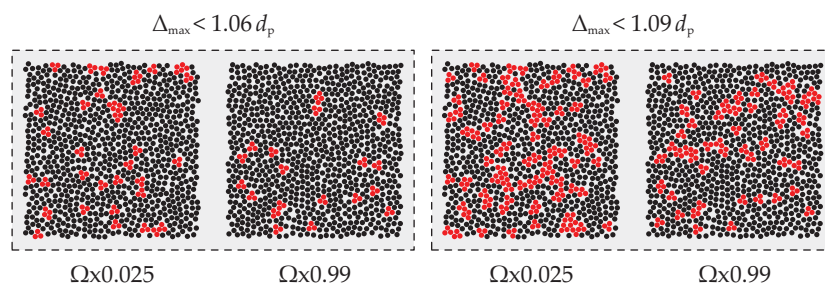


Figure 2: Bulk random packings of 900 monosized hard disks at $\epsilon \approx 0.34$ generated with the MC-based algorithm using different compression rates ($\Omega \times 0.025$ and $\Omega \times 0.99$ packings) in the packing protocol. Red disks form closely packed (quasi-crystalline) regions according to the value of Δ_{\max} , which is indicated above the gray blocks. Lower values of the compression rate ($\Omega \times 0.025$ packings) result in a larger fraction of dense regions, which translates to a higher DoH for the generated packings due to a maldistribution of the available void space.

shown in Fig. 2. Closely-packed regions were identified by *Delaunay triangulation* [17] performed on the disk centers. Closely packed disks (marked in red) form close-to-regular triangles on the Delaunay mesh and can be identified according to the criterion of maximal edge length Δ_{\max} , i.e., disks forming triangles with a maximal edge length shorter than Δ_{\max} are assumed as closely packed. At equal bed porosity, a packing with a larger fraction of densely packed spheres has a higher DoH than a packing with a lower fraction of dense regions due to a higher maldistribution of the available void space [10].

For this study, unconfined packings of uniform hard spheres with diameter d_p were generated in a rectangular box of about $10 d_p \times 10 d_p \times 70 d_p$ with periodic boundary conditions at its faces. Each packing contained about $7 \cdot 10^3$ spheres, the exact amount depending on the packing void fraction, where the range between random-close and random-loose packing was covered ($\varepsilon = 0.366-0.46$). Four JT- (Rx0.001, R, S, and Sx2) and two MC-based packing types ($\Omega \times 0.95$ and $\Omega \times 0.05$) were generated at each of the following bed porosities: $\varepsilon = 0.366, 0.38, 0.40, 0.42, 0.44$, and 0.46 , except for the Sx2-packing, for which JT generation did not converge for the lowest bed porosity of 0.366 . Ten random realizations of each packing were generated to account for statistical variations in the microstructure of a packing with defined DoH and bed porosity.

3 Simulation of fluid flow

For the simulation of low-Reynolds number flow ($Re = d_p u_{av} / \nu \sim 10^{-3}$, where u_{av} is the average flow velocity and ν is the kinematic viscosity) of an incompressible fluid through the packing void space, the packings are discretized on a uniform cubic grid, marking each voxel as solid or fluid according to the spatial position of its geometrical center, inside or outside the closest sphere, respectively. The flow simulation is based on the LBM, used with the BGK collision operator, the D3Q19 lattice, and a bounce-back rule applied at the solid-liquid interface [18]. Simulations are performed at low Mach number ($Ma \sim 10^{-3}$), with fixed lattice (kinematic) viscosity $\nu = 1/6$ (this corresponds to the relaxation parameter $\tau = 1$, which was shown to provide an accurate performance for the employed scheme [19]), and a body force approach [20] to drive the fluid through the packing. Values of the pressure gradient were chosen from 10^{-7} (in lattice units) at a resolution of $90 \text{ nodes}/d_p$ to 10^{-4} at $10 \text{ nodes}/d_p$, which keeps small the numerical error due to the employed realization of the forcing term [21].

4 Simulation of hydrodynamic dispersion

4.1 Advection-diffusion equation

The classical advection-diffusion equation (ADE) states that in the absence of sources the evolution of a solute concentration $C(\mathbf{x}, t)$ within a control volume is given by the

diffusive and advective fluxes entering this volume

$$\frac{\partial C}{\partial t} = \nabla \cdot (\mathbf{D} \nabla C) - \nabla \cdot (\mathbf{v} C), \quad (4.1)$$

where $\mathbf{v}(\mathbf{x}, t)$ is the fluid velocity and \mathbf{D} is the diffusion tensor [1]. The combination of parabolic and hyperbolic differential equations [22] makes a numerical solution of Eq. (4.1) difficult, because a discrete version of this equation changes its nature from parabolic to hyperbolic as advection starts to dominate diffusion [23]. Discrete schemes based on a solution of Eq. (4.1) suffer from mass loss, oscillating solutions, and numerical dispersion [24–27], the latter yielding artificially distorted concentration profiles in advection-dominated flow regimes. The large difference often observed between transverse and longitudinal dispersion coefficients [28] aggravates this problem.

Although numerical solution of the ADE is often stated as being unable to reproduce non-Fickian behavior of the hydrodynamic dispersion coefficient, the opposite has been demonstrated if the spatial heterogeneities of porous media are resolved at the pore level [29]. This underlines the importance of pore-scale transport processes for the macroscopic mass transport in porous media.

4.2 Random-walk particle-tracking method (RWPT)

Contrary to the Eulerian methods mentioned above, RWPT is a Lagrangian approach that does not solve the ADE (Eq. (4.1)) directly. The basic concept of RWPT is to simulate solute transport as the motion of a large number of fictitious particles, referred to as an ensemble of inert tracers [30–32]. The tracers have point-like dimension and no mass, and they are inert in the sense that they neither interact with each other nor adsorb to the surface of the porous medium nor affect the motion of the fluid. Time evolution of a tracer results from drift due to the underlying flow field and Brownian motion due to molecular diffusion. This is described by a stochastic differential equation:

$$d\mathbf{r}(t) = \mathbf{v}(\mathbf{r}(t))dt + \mathbb{B}d\mathbf{W}(t), \quad (4.2)$$

where $\mathbf{r}(t)$ and $\mathbf{v}(\mathbf{r}(t))$ are the tracer coordinates and the fluid flow velocity at this location, \mathbb{B} is a second-order tensor with non-zero diagonal elements equal to $\sqrt{2D_m}$ (with D_m as molecular diffusion coefficient), and $d\mathbf{W}(t)$ is an increment of the vector Wiener process (often called Brownian motion). The connection between Eq. (4.2), the Fokker-Planck equation, and the ADE is described in [32].

In the general case, Eq. (4.2) cannot be solved analytically. The simplest and often used [33, 34] numerical solution of Eq. (4.2) employs a one-step Euler approximation in the following form [35]

$$\mathbf{r}(t + \Delta t) = \mathbf{r}(t) + \mathbf{v}(\mathbf{r}(t))\Delta t + \sqrt{2D_m \Delta t} \mathbf{N}, \quad (4.3)$$

where Δt is the time step and \mathbf{N} a vector with random components following a normal distribution with zero mean and unity variance. A sequence of normally distributed

pseudo-random numbers generated by digital computers can be used to approximate the Wiener process increment $d\mathbf{W}$ and thus to serve as the components of \mathbf{N} [35].

Tailing of the normal distribution may produce random numbers with a value in the infinite range. To avoid very large values for the diffusive tracer displacement, we use a truncated normal distribution for random-number generation: the maximal value for diffusive tracer displacement does not exceed $4\sqrt{D_m\Delta t}$, which is sufficiently large to render the truncation error negligible [36].

The advantages of RWPT for our purpose are mass conservation (due to a constant number of tracers in the simulation domain), absence of numerical dispersion, and the simplicity of the program realization and its further parallelization. Compared with methods based on the solution of the ADE, RWPT simulations of mass transport in systems with simple solid-liquid geometries (for example, dispersion in an open tube) need higher computational times, but in systems with complex solid-liquid boundaries, like the random sphere packings studied here, the opposite is true [27, 37]. In our study we do not operate with the spatial concentration profiles; if the accurate reproduction of concentration profiles is of interest, then RWPT may not be the best choice because a large amount of tracers is required [37].

At the start of the RWPT simulation, the tracers are randomly distributed in the whole packing void space. This initial condition enables a faster data collection with respect to spatial heterogeneity and the intrinsic DoH of a packing than the plane-wise deposition of tracers at the inlet (which would correspond to a simulation of pulse-injection experiments).

4.3 Program realization

The program realization of LBM and RWPT methods was implemented as parallel codes in C/C++ languages using the Message Passing Interface standard. The details of the program realization and scaling of parallel performance of the codes can be found elsewhere [38, 39]. In this study the largest simulation domain had dimensions of about $900 \times 900 \times 13\,500$ lattice nodes ($10 d_p \times 10 d_p \times 150 d_p$; cf. Fig. 4); in such a domain simulation of the flow field took about 2.1 hours while simulation of hydrodynamic dispersion at one average velocity required 0.15 hours on 4096 processor cores of a BlueGene[®]/P system.

4.4 Hydrodynamic dispersion coefficient and Péclet number

The time-dependent hydrodynamic dispersion coefficient along the z -direction is calculated as the rate of spreading of a tracer ensemble as

$$D_z(t) = \frac{1}{2N_{\text{tr}}} \frac{d}{dt} \sum_{i=1}^{N_{\text{tr}}} (\Delta z_i(t) - \langle \Delta z_i(t) \rangle)^2, \quad (4.4)$$

where N_{tr} is the number of tracers, $\Delta z_i(t)$ is the displacement in z -direction of the i -th tracer at time t , and $\langle \Delta z_i(t) \rangle$ is the average displacement in z -direction of the whole tracer ensemble [40]. In our study, the hydrodynamic dispersion coefficient is calculated along two principal directions, parallel and orthogonal to the macroscopic flow direction, and denoted as longitudinal (D_L) or transverse (D_T) dispersion coefficient, respectively. The calculated values are normalized by the molecular diffusion coefficient of the tracer, D_m ; the normalized values $D_z(t)/D_m$ reflect the ratio between the rate of tracer spreading in the packing void space due to hydrodynamic dispersion and the rate of spreading due to molecular diffusion in bulk solution. In our study, $D_z(t)/D_m$ takes values from close to unity up to several hundreds, depending on the particular packing, the direction along which dispersion is calculated, and the average flow velocity.

Flow of an average velocity u_{av} through a porous material can be characterized by the Péclet number

$$Pe = \frac{u_{\text{av}} l_c}{D_m}, \quad (4.5)$$

which relates advective to diffusive transport in a system with a characteristic dimension l_c (for sphere packings $l_c \equiv d_p$). Mass transport becomes diffusion-limited for $Pe < 1$ and advection-dominated if $Pe \approx 10$ or higher (although the contribution of diffusion cannot be neglected). An in-depth study of the hydrodynamic dispersion characteristics of random sphere packings requires simulations over a wide range of Péclet numbers to distinguish between individual dispersion contributions and their characteristic velocity dependence [28]. The typical flow regime in dense porous media is low-Reynolds-number flow ($Re \ll 1$), also known as creeping or Stokes flow. According to Darcy's law [1], the pressure gradient driving the flow and the average flow velocity are directly proportional as long as $Re \ll 1$ is satisfied [41], and the local flow vector components follow the same linear scaling [42, 43]. This allows to calculate the flow field for a given packing at low Reynolds number ($Re < 0.01$) and then realize the required Péclet numbers by linear rescaling of the flow field components.

4.5 Boundary conditions

The no-flux boundary condition (BC) at the solid-liquid interface was implemented using the multiple-rejection scheme, which effects that each tracer move that crosses the solid-liquid interface is rejected and the diffusive component of the tracer displacement recalculated until the tracer move remains strictly in the fluid phase. Multiple rejection has been shown to lead to artificially distorted concentration profiles near the solid-liquid interface, as opposed to the more precise, but computationally expensive specular reflection scheme [36]. To investigate the influence of the numerical error introduced by the multiple rejection BC on the simulated hydrodynamic dispersion coefficients, we performed simulations [38] in which the time step was varied from a particular default value of Δt to $\Delta t_{0.1} = 0.1\Delta t$ and $\Delta t_{0.02} = 0.02\Delta t$. The default time step Δt was chosen such that the maximal advective-diffusive displacement of a tracer does not exceed half of the lattice-

spacing Δx . A smaller time step results in a reduced influence of the multiple rejection BC on the tracer motion and thus on the hydrodynamic dispersion coefficient. These test simulations were performed for a bulk random sphere packing at the random-close packing limit ($\varepsilon = 0.366$), for which the error introduced by the multiple-rejection BC is assumed to be the largest. Performing simulations at $Pe = 500$ and a discretization resolution of 30 nodes/ d_p , we found only 3% difference in the asymptotic values of the dispersion coefficient between Δt and $\Delta t_{0.02}$ [38]. Our findings are in agreement with the results previously reported by Maier et al. [33].

4.6 Hydrodynamic dispersion in an open channel

We begin the validation of our RWPT approach with a simple geometry, for which an analytical solution to calculate the hydrodynamic dispersion coefficient is available: an open channel with circular cross-section (cylindrical channel). Dispersion in an open channel, also known as Taylor-Aris dispersion [44,45] can be quantified as:

$$\frac{D_L}{D_m} = 1 + \frac{Pe^2}{210} f, \quad (4.6)$$

where f is a function that depends on the geometry of the open channel [46]: $f = 1$ for parallel plates and $f = f_{\text{cir}} = 210/192 \approx 1.09$ for a cylindrical channel. The simulation domain was discretized at 25 nodes/ l_c , with the cylinder radius as the characteristic dimension l_c . Fig. 3(a) shows the normalized longitudinal dispersion coefficient $D_L(t)/D_m$ as a function of the diffusive time $\tau_{\text{diff}} = t2D_m/l_c^2$. The dispersion curve contains a pre-asymptotic or transient part, in which the dispersion coefficient undergoes rapid increase, and an asymptotic part, in which the value stays approximately constant. The growth of $D_L(t)/D_m$ in the transient part is a result of the difference between convective ($\sim t$) and diffusive ($\sim \sqrt{t}$) tracer displacements: at very short times ($\tau_{\text{diff}} \ll 1$), the solute is spread mainly due to diffusion and $D_L(t)/D_m$ is close to 1. With increasing simulation time, the nonuniform displacement of the solute originating from a nonuniform flow

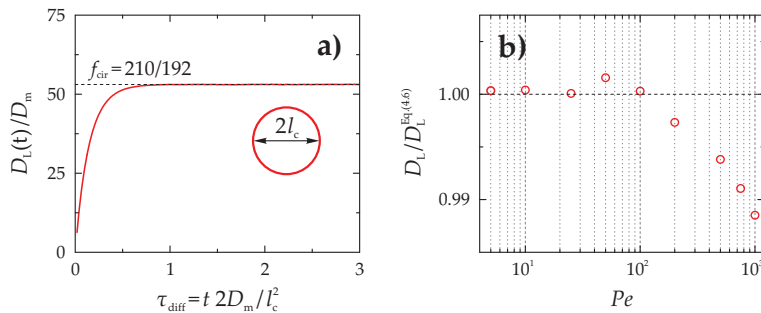


Figure 3: a) Time evolution of the hydrodynamic dispersion coefficient in an open channel with circular cross-section at $Pe = 100$. b) Asymptotic values of the dispersion coefficient normalized by its theoretical value calculated using Eq. (4.6) with $f_{\text{cir}} = 210/192$.

field leads to the growth of $D_L(t)/D_m$; after the tracers have explored the longest distance between the different velocities of the flow field (which in the studied system are located near the channel wall and at its center), asymptotic behavior of $D_L(t)/D_m$ is observed. The theoretical values for the asymptotic normalized hydrodynamic dispersion coefficient D_L/D_m calculated with Eq. (4.6) are indicated in Fig. 3(a) by a dashed line; our simulated values show excellent agreement with the theoretical prediction for the open channel at $Pe = 100$. Fig. 3(b) shows the deviation of the simulated dispersion coefficients from the corresponding analytical values as a function of Péclet number for $5 \leq Pe \leq 1000$, demonstrating a low numerical error for all studied Pe values.

4.7 Influence of the packing length on the hydrodynamic dispersion coefficient

Whereas simulations in ordered packings can be performed in the smallest repetitive unit of the structure (e.g., the unit cell of a crystal), the appropriate choice of domain size or packing dimensions is not trivial for random packings. Fig. 4 shows how the chosen packing length affects the simulated hydrodynamic dispersion coefficient of a dense random sphere packing ($\varepsilon = 0.366$). For this study, we used a JT-packing, because the microstructures of the JT-generated packings at $\varepsilon = 0.366$ (R \times 0.001, R, and S) are highly similar, due to the severe space restrictions put by the random-close packing limit on the possible placement of spheres in the packing. As a consequence, the DoH and thus the hydrodynamic dispersion coefficient of the JT-packings converge to a minimum at the random-close packing limit ($\varepsilon = 0.366$) [9]. (The same does not apply to the MC-packings [10].) At lateral packing dimensions of $10 d_p \times 10 d_p$, the packing length was varied as $L = 6, 15, 25, 75$, and $150 d_p$. We used a high spatial resolution of 90 nodes/ d_p for discretization to eliminate the possible influence of insufficient grid resolution on the study. Simulations were performed at high flow velocity ($Pe = 500$), where the effect of insufficient packing length is most apparent. The time evolution curves for the hydrodynamic dispersion coefficient in Fig. 4 converge at a packing length of $75 d_p$; increasing the packing length up to $150 d_p$ does not improve the simulation result further. Packing lengths $< 75 d_p$ yield distorted dispersion curves. This results when the longitudinal displacement of some tracers exceeds the packing length, so that some flow paths are explored more than once due to the periodic boundary conditions. To avoid these recorelation effects the simulation domain must be long enough. Values of $(L/d_p)/\tau_{\text{conv}} = 2-4$ were previously suggested for the minimal domain length [33,47]. At longer evolution times (larger values of τ_{conv} than shown in Fig. 4) close-to-asymptotic behavior was attained for *all* tested packing lengths, which demonstrates that observation of asymptotic behavior does not guarantee the absence of recorelation effects. If periodic boundary conditions are not applied, an insufficient packing length according to the criterion above will put the simulated hydrodynamic dispersion coefficient into the transient regime, where the relative difference between simulated and asymptotic value of the dispersion coefficient increases steeply with the flow rate (cf. Fig. 13 in [33]). This introduces an

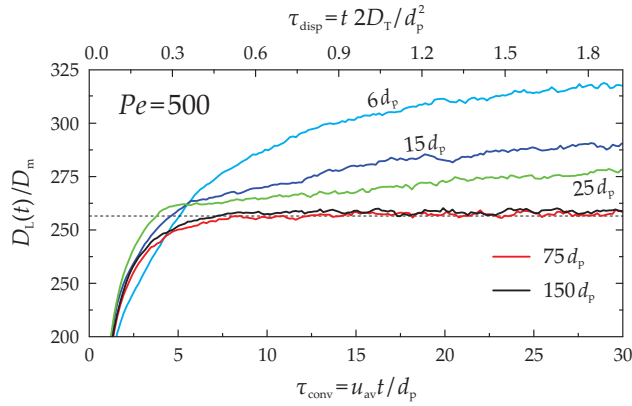


Figure 4: Evolution of the hydrodynamic dispersion coefficient for a bulk random sphere packing as a function of convective τ_{conv} and dispersive τ_{disp} time. $\tau_{\text{conv}} = u_{\text{av}} t / d_p$, where u_{av} is the average flow velocity and d_p is the sphere diameter. $\tau_{\text{disp}} = 2D_T t / d_p^2$, where D_T denotes the time-independent transverse dispersion coefficient. Simulations were performed at $Pe = 500$ in a dense R-packing ($\varepsilon = 0.366$) discretized with a spatial resolution of $n = 90$ grid nodes per sphere diameter. At lateral dimensions of $10 d_p \times 10 d_p$, the packing length was varied between 6, 15, 25, 75, and $150 d_p$.

additional difficulty for comparison with dispersion data from other studies; however if one is aware of this problem, a qualitative comparison is still possible. Nevertheless, asymptotic values of the dispersion coefficient are required for comparison with theoretical predictions [28].

4.8 Influence of the grid resolution on the hydrodynamic dispersion coefficient

The influence of the grid resolution (n , in lattice nodes/ d_p) on the hydrodynamic dispersion coefficient was evaluated for the Rx0.001-packing type, because we expect the effects of insufficient grid resolution to be strongest for the most heterogeneous packing microstructure. At the lower limit of bed porosities ($\varepsilon = 0.366$), the DoH of the Rx0.001-packing and its hydrodynamic dispersion coefficient are quasi-identical to those of the other JT-packing types at this bed porosity (R and S). But the DoH of the Rx0.001-packing type increases stronger than those of the other packing types with the bed porosity, so that at the random-loose packing limit ($\varepsilon = 0.46$), the Rx0.001 packing has the largest DoH and hydrodynamic dispersion coefficient among the generated packing types [9]. For packing dimensions of $10 d_p \times 10 d_p \times 75 d_p$, the grid resolution was varied from $n = 10$ to $n = 90$. Asymptotic values of the dispersion coefficient were estimated as its average value between 2 and 4 dispersive times τ_{disp} [28]. Fig. 5(a) displays the error in the dispersion coefficient simulated at lower grid resolutions relative to the dispersion coefficient simulated at the highest grid resolution ($n = 90$) for low ($Pe = 5$), moderate ($Pe = 50$), and high ($Pe = 500$) flow velocities. At lower grid resolution ($n \leq 30$) the relative error values decrease monotonously, but deviate from the monotonous trend when the relative

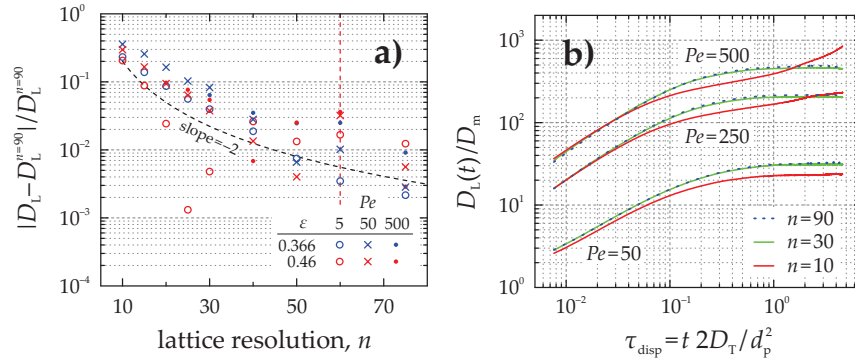


Figure 5: a) Dependence of the relative error in asymptotic values of the hydrodynamic dispersion coefficient on the grid resolution at $Pe=5, 50,$ and 500 in $Rx0.001$ packings with a porosity as indicated in the figure legend. b) Evolution of the hydrodynamic dispersion coefficient in a bulk packing ($Rx0.001, \varepsilon=0.46$) at low ($n=10$), moderate ($n=30$), and high ($n=90$) grid resolution as a function of the transverse dispersive time, $\tau_{\text{disp}}=2D_T t/d_p^2$. Because for some of the studied packings asymptotic behavior of the dispersion coefficient was not observed at $n=10-25$ and $Pe=500$, the respective data were not included in panel a).

error reaches values of $\sim 10^{-2}$. The latter can be attributed to low-frequency oscillations of the time-dependent dispersion curve, whose amplitudes are more pronounced in looser packings ($\varepsilon=0.46$) with higher maldistribution of the void space. The slope of convergence depends on several factors that are influenced by the grid resolution: i) The stair-step representation of the spheres' contours in the packing approaches smooth boundaries closer with higher grid resolution. ii) The accuracy of the bed porosity for a discretized packing increases with the grid resolution. iii) The local error introduced by the bounce-back scheme (used with D3Q19 BGK LBM [48]) near the boundary of each sphere decreases with the grid resolution. iv) The error introduced by the zero-order approximation (flow velocity is assumed to be constant over a lattice voxel) used to calculate advective tracer displacement decreases with the grid resolution. v) The tracer displacement relative to the sphere diameter d_p (as mentioned before, the maximal tracer displacement does not exceed half the lattice spacing) decreases with the grid resolution. Under consideration of the available computational resources, we employed a resolution of $n=60$ in further simulations. According to Fig. 5, the relative (to $n=90$) numerical error of the simulated dispersion coefficients introduced by the chosen grid resolution is about 10^{-2} .

At low grid resolution ($n=10-25$) the high-velocity data ($Pe=500$) are missing in Fig. 5(a). This issue is addressed in Fig. 5(b), where we present the time evolution of the hydrodynamic dispersion coefficient at $Pe=50, 250,$ and 500 for grid resolutions of $n=10, 30,$ and 90 . The use of the dispersive time scale τ_{disp} allows to relate the transient time of the hydrodynamic dispersion coefficient to its time-independent value, because in bulk random sphere packings close-to-asymptotic behavior of the hydrodynamic dispersion coefficient is observed after $\tau_{\text{disp}} \approx 1-2$, independent from the Péclet number [28]. The dispersion coefficients simulated at moderate flow velocity ($Pe=50$) reach their close-

to-asymptotic value after $\tau_{\text{disp}} \approx 1$ for all grid resolutions. This also holds for higher Péclet numbers ($Pe = 250, 500$) and grid resolutions of $n = 30, 90$. Qualitatively different behavior is observed at low spatial resolution ($n = 10$), where for higher Péclet numbers the dispersion coefficients diverge after $\tau_{\text{disp}} \approx 1$, and the corresponding divergence rate increases with the Péclet number (cf. red curves at $Pe = 250$ and $Pe = 500$ in Fig. 5(b)). This behavior of D_L/D_m was also observed at high Péclet numbers by Maier et al. [33] (see Fig. 13 in their work).

The aforementioned divergence of the dispersion coefficients was reported by Lowe and Frenkel [47] (and later commented on by Koch et al. [49] and Maier et al. [33]), who simulated advective-diffusive transport in a bulk random sphere packing with dimensions of $10 d_p \times 10 d_p \times 28 d_p$, a bed porosity of 0.55, and discretized at grid resolutions of $n = 5$ and $n = 9$. They used LBM and the moment propagation method [51] to simulate flow and dispersion, respectively. (The authors analyzed the time evolution of the longitudinal dispersion coefficient $D_L(t)$ by the velocity autocorrelation function $C_L(t)$, which is related to the former through $D_L(t) = \int_0^t C_L(t') dt'$.) Observing a time behavior as indicated by the red lines in Fig. 5(b), these authors [47] questioned the existence of hydrodynamic dispersion coefficients. Maier et al. [33] argued that the divergence of the dispersion coefficients in the work of Lowe and Frenkel [47] could arise from numerical dispersion caused by the moment propagation method. However, as Fig. 5(b) shows, a poorly resolved simulation domain may also contribute to the observed divergence of the dispersion coefficients.

5 Comparison of hydrodynamic dispersion coefficients with literature data

Fig. 6 shows asymptotic values of the dispersion coefficient $D_L(t)/D_m$ for the generated six sphere packing types (JT-packings: Rx0.001, R, S, Sx2; MC-packings: $\Omega \times 0.05$, $\Omega \times 0.95$) over the whole bed porosity range ($\varepsilon = 0.366-0.46$). Statistical variations in our simulated dispersion coefficients are given by the standard error of the mean, calculated from ten random realizations of each packing. The low values for the standard error prove that differences between individual packings of a given type and bed porosity are smaller than differences between the packing types. This was our goal with the different packing types: to introduce a systematic variation of a packing's DoH which is reflected in the dispersion coefficients. Each packing type (Rx0.001, R, S, Sx2, $\Omega \times 0.05$, $\Omega \times 0.95$) demonstrates a distinct porosity-dependence of the dispersion coefficient. For example, the dispersion coefficient of the $\Omega \times 0.95$ MC packing type is almost independent of the porosity (this was also mentioned in other studies where the MC algorithm was employed for packing generation [47, 52]), whereas in the Rx0.001 JT packing type the dispersion coefficient increases strongly with the porosity. The porosity-dependence of the dispersion coefficients scales with the DoH of the generated packings, as quantified by statistical analysis of a geometrical measure derived by Voronoi tessellation [9, 10].

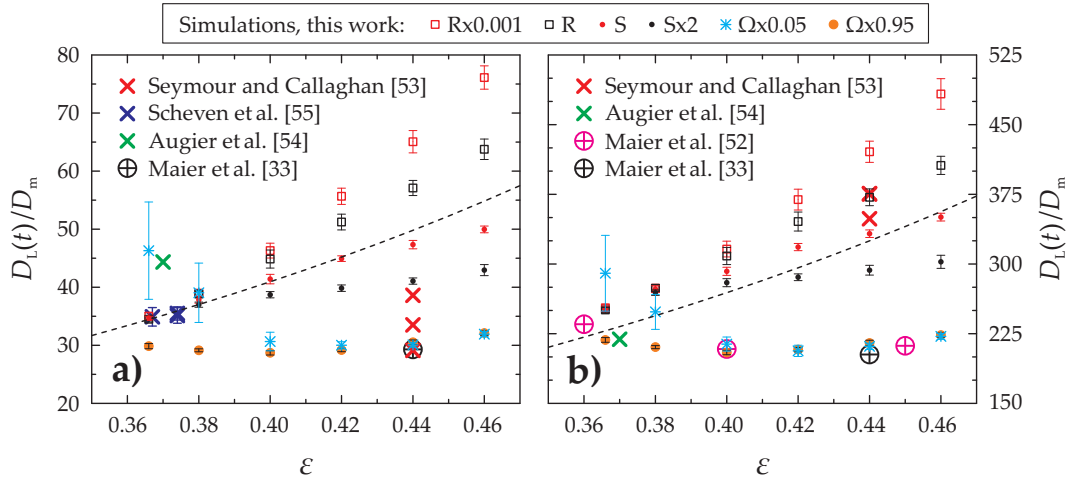


Figure 6: Asymptotic values of the hydrodynamic dispersion coefficient from i) LBM and RWPT simulations in bulk packings generated with JT (R- and S-packings) and MC (Ω -packings) algorithms, ii) NMR measurements of Seymour and Callaghan [53], iii) NMR measurements of Scheven et al. [55], iv) LBM and RWPT simulations of Maier et al. [33, 52] in sphere packings generated with the MC-algorithm, and v) simulations of Augier et al. [54] based on the solution of the ADE in a packing generated with the discrete element method. Results are shown for a) $Pe=100$ and b) $Pe=500$. The dashed line denotes the correlation proposed by Scheven et al. [55] (Eq. (5.1)). Error bars for our simulations indicate 95% confidence intervals calculated using dispersion values from 10 random realizations of each packing of a given type and porosity. Error bars for the data of Scheven et al. [55] were digitized from their publication.

We compared our simulated dispersion coefficients at $Pe = 100$ (Fig. 6(a)) and $Pe = 500$ (Fig. 6(b)) with i) data from NMR measurements of Seymour and Callaghan [53], ii) dispersion coefficients from the simulations of Augier et al. [54], which are based on the numerical solution of Navier-Stokes and advection-diffusion equations, iii) dispersion coefficients simulated by Maier et al. [33, 52] in computer-generated sphere packings, and iv) NMR data of Scheven et al. [55]. The hydrodynamic dispersion data in these studies refer to a range of bed porosities and fluid velocities. For comparison at equal Pe , we scaled the original values of the dispersion coefficients D_L/D_m given by the authors at a certain Pe to the respective value of D_L/D_m at $Pe = 100$ (Fig. 6(a)) or $Pe = 500$ (Fig. 6(b)), using either the $D_L(Pe)/D_m$ correlations proposed by the authors themselves or, when such a correlation was not given, the widely accepted power law scaling $D_L(Pe)/D_m \sim Pe^\beta$, with $\beta = 1.2$ [56]. For clarity, the authors' original hydrodynamic data (Pe , D_L/D_m), bed porosities, and the scaled values used in our comparison (Fig. 6), together with the employed scaling law, are summarized in Table 1.

The NMR measurements of Seymour and Callaghan [53], whose data are shown as red crosses in Fig. 6, were performed in a confined cylindrical packing with a cylinder-to-particle diameter ratio of ~ 21 and a bed porosity of $\varepsilon = 0.44$. As we have previously shown [28], the *asymptotic* dispersion coefficient of a packing confined in a cylinder of such lateral dimensions is several times larger than that of a bulk packing of similar bed porosity, and the time required to reach asymptotic values of the dispersion coefficient

Table 1: Dispersion coefficients (D_L/D_m) taken from the literature. Original values given at a certain Péclet number were scaled to $Pe=100$ (Fig. 6(a)) and $Pe=500$ (Fig. 6(b)) for comparison with our simulated data.

Original study	ε	Pe		D_L/D_m		Scaling law
		original	scaled	original	scaled	
Seymour and Callaghan [53]	0.44	68	100	22.5	38.6	$D_L/D_m \sim Pe^{1.37}$
		99	100	32.8	33.5	
		134	100	43.4	29.1	
		340	500	221	375	
		400	500	257	349	
		811	500	732	377	
Augier et al. [54]	0.37	70	100	31.4	44.3	$D_L/D_m \sim Pe^{1.0}$
		1464	500	630	219	
Maier et al. [33]	0.44	95	100	28	29	$D_L/D_m \sim Pe^{1.2}$
		476	500	191	203	
Maier et al. [52]	0.36	476	500	222	235	$D_L/D_m \sim Pe^{1.2}$
		476	500	197	208	
		476	500	200	212	
Scheven et al. [55]	0.367	85.9	100	29.1	34.9	$D_L/D_m \sim Pe^{1.2}$
		87.0	100	30.0	35.5	
		130.9	100	48.5	35.1	

is even two orders of magnitude larger compared with the bulk packing. Seymour and Callaghan presented data from two sets of NMR measurements, with $\Delta = 10$ ms and $\Delta = 30$ ms (where Δ is the experimental observation time in their pulsed field gradient NMR measurements). In Fig. 6, we present dispersion coefficients measured after a time of $\Delta=30$ ms, which corresponds to a convective time of $\tau_{\text{conv}}=u_{\text{av}}t/d_p \approx 0.8$ and $\tau_{\text{conv}} \approx 4.0$ for $Pe = u_{\text{av}}d_p/D_m = 100$ (Fig. 6(a)) and $Pe = 500$ (Fig. 6(b)), respectively. At these values of convective time and Péclet number the dispersion coefficient of even a *bulk* packing at $Pe=100$ and $Pe=500$ (for the corresponding time scales see, for example, Fig. 13 in [33]) is still in the transient regime. Maier et al. [57] demonstrated that at such short observation times the dispersion coefficient of a confined packing is close to that of a bulk packing with similar properties, which are defined by the packing protocol and bed porosity. Hence, the data of Seymour and Callaghan [53] acquired with $\Delta = 30$ ms correspond to dispersion values from the bulk region of their packing, and the observed dispersion coefficient is closer to the asymptotic value at $Pe = 500$ than at $Pe = 100$. This agrees with the shift of their data in Fig. 6 (red crosses) from the lower range of the dispersion coefficients at $Pe = 100$ (Fig. 6(a)) to the upper range at $Pe = 500$ (Fig. 6(b)).

The simulations of Augier et al. [54] (Fig. 6, green crosses) were performed in a bulk packing extracted from the central region of a confined cylindrical packing with a cylinder-to-particle diameter ratio of ~ 24 . The confined polydisperse sphere packing

was generated with the discrete element method [58]. The actual aspect ratio of the cylindrical packing (~ 24) and the polydispersity of spheres resulted in a relatively low bed porosity of 0.33. Flow and mass transport problems were solved using traditional computational approaches based on the numerical solution of Navier-Stokes and advection-diffusion equations. We therefore included the work of Augier et al. [54] (Table 1, Fig. 6) as it is insightful to compare very similar transport problems solved by fundamentally different simulation approaches. The numerical methods employed by Augier et al. [54] require tessellation of the interparticle void space and sphere surfaces into a set of irregular space elements. The authors reported an inability of their software to perform the space tessellation for the original packing with touching spheres. Therefore, each sphere of the generated packing was contracted by 2% of its diameter, which increased the bed porosity to 0.37. Fig. 6 shows moderate agreement of our simulated data with those of Augier et al. [54]: the value of D_L/D_m at $Pe = 100$ (Fig. 6(a)) corresponds to the dispersion coefficient we simulated for $\Omega \times 0.05$ packings, while the value of D_L/D_m at $Pe = 500$ (Fig. 6(b)) corresponds to the dispersion coefficient we simulated for the $\Omega \times 0.95$ packings. This may not be attributed to possible numerical artefacts of ADE-based solvers or numerical dispersion (because the latter would increase the hydrodynamic dispersion coefficient as the Péclet number grows), but can be explained by the following differences between our simulations and those of Augier et al. [54]: i) packings of monodisperse spheres *vs.* packings of polydisperse spheres, ii) true bulk packings with periodic boundary conditions *vs.* bulk packings cut from larger confined packings and with “symmetric planes” lateral boundary conditions, and iii) low Reynolds number ($Re \ll 1$) *vs.* moderate Reynolds number ($1 < Re < 100$) flow.

Maier et al. [33,52] performed simulations of hydrodynamic dispersion in bulk sphere packings generated with the MC algorithm (the corresponding dispersion coefficients are shown in Fig. 6 as black and magenta crosses). Low Reynolds number flow and mass transport were simulated using LBM and RWPT. The authors took care to observe asymptotic time behavior of the dispersion coefficient, which is free from finite size or numerical artifacts. The similarity of our and Maier’s packing generation allows a comparison of the dispersion coefficients between bulk packings of similar microstructures. Maier et al. [52] reported a weak dependence of the dispersion coefficients on bed porosity (within a range of $\varepsilon = 0.36-0.50$) if a low compression rate ($\Omega \times 0.05$) was used for packing generation (see Section 2 for the description of the MC algorithm). This behavior observed by Maier et al. [52] is represented by the magenta crosses in Fig. 6(b). These data compare excellently with the dispersion coefficients obtained for our MC-packings at porosities $\varepsilon \geq 0.40$. Yet, at porosities $\varepsilon < 0.40$ and low compression rate ($\Omega \times 0.05$) we observe a stronger dependence of the dispersion coefficients on the bed porosity than in the work of Maier et al. [52], whereas MC-packings obtained at high compression rate ($\Omega \times 0.95$) remain little affected with respect to the resulting dispersion. We have recently analyzed the microstructure of these MC-packings (and the JT-packings) by spatial tessellation techniques and found that at low bed porosities the $\Omega \times 0.05$ packings are characterized by a higher nonuniformity in the distribution of the interparticle void space (see,

e.g., Fig. 5 in [10]). This is also illustrated by Fig. 2: the lower compression rate results in a larger fraction of dense regions, which translates to a higher DoH due to a maldistribution of the available void space. The difference in the microstructures (and corresponding dispersion coefficients) between our and Maier's MC-packings may originate from a different number of iterations (N_{it}) before compression of the simulation box is executed. In our study $N_{it} = 5000$ while Maier et al. [33, 52] did not mention the value of N_{it} in their study. To summarize, Fig. 6 shows excellent agreement of the hydrodynamic dispersion coefficients simulated for the $\Omega \times 0.95$ packings with the data of Maier et al. [33, 52].

Dark blue crosses in Fig. 6(a) denote the NMR data from Scheven et al. [55]. The NMR measurements were performed in cylindrical columns with a cylinder-to-particle diameter ratio of ~ 375 and bed porosities of $\varepsilon = 0.367$ and 0.374 . The observation time was long enough ($\tau_{conv} > 20$) to observe close-to-asymptotic behavior of the dispersion coefficients for the *bulk* region of these packings. According to Fig. 6(a), our simulation results agree excellently with those data.

Scheven et al. [55, 59] suggested the existence of an *intrinsic* value of the dispersion coefficient for bulk random sphere packings. They stated that dispersion in an unconfined sphere packing is defined solely by the Péclet number and the hydrodynamic radius (r_h) of a packing ($r_h = (1/6)d_p\varepsilon/(1-\varepsilon)$), and proposed the following equation (dashed lines in Fig. 6):

$$\frac{D_L}{D_m} = Pe_{eff}(A \ln(Pe_{eff}) + B), \quad (5.1)$$

where $Pe_{eff} = 6u_{av}r_h/D_m = Pe\varepsilon/(1-\varepsilon)$, $A = 0.12 \pm 0.007$, and $B = 0.11 \pm 0.03$ (in later work [59] Scheven suggested $A = 0.131 \pm 0.007$ and $B = 0.07 \pm 0.03$ for $10 \leq Pe_{eff} \leq 2100$). According to the authors, Eq. (5.1) specifies the *lower* bound for dispersion values in bulk packings, and higher dispersion coefficients, if they are observed, are caused by factors not related to the packing microstructure, such as nonuniform injection of a tracer plug or faster flow near the confining wall where the bulk random-dense packing microstructure is distorted. However, our results in Fig. 6 demonstrate that the dispersion coefficients of bulk random sphere packings take values that are significantly lower or higher than predicted by Eq. (5.1). Fig. 6 also reveals that any correlation for random sphere packings in the form of $D_{ax}/D_m = f(Pe, \varepsilon)$ will fail to provide precise results if it does not take the microstructural DoH of the packings into account.

Scheven et al. [55] confirmed the validity of Eq. (5.1) by comparison with their NMR data, theoretical predictions of Saffman [60, 61] (which are based on the capillary model), and simulations of Maier et al. [33]. Fig. 6 shows that Maier's data are approximately 3/2 times lower than predicted by Eq. (5.1). Probably, this fact led the authors to assume the hydrodynamic radius r_h of Maier's packings to be 3/2 times lower than r_h of "smoothed" spheres (due to the discrete representation of the packing spheres on a cubic lattice), and to upscale Maier's data accordingly. Maier and Bernard [48] in their later study introduced the smooth representation of sphere surfaces and found that this results in *lower* values of the dispersion coefficient, which contradicts the assumption of Scheven et al. [55]. The homogeneous microstructure (low DoH) of the MC-packings used by

Maier et al. [33, 52] yielded probably the lowest dispersion coefficients for bulk random sphere packings reported in the literature [55, 62].

6 Conclusion

In this study we generated random packings of monodisperse, hard spheres with different bed porosities ($\varepsilon = 0.366-0.46$) and degree of heterogeneity (DoH). Variation of DoH was achieved by variation of the packing protocol, using different parameters settings as well as two algorithms, Jodrey-Tory and Monte Carlo, and resulted in six distinct packing types (Rx0.001, R, S, Sx2, Ω x0.05, Ω x0.95). Each packing was generated ten times to address the influence of the random realization on the transport properties. We employed LBM and RWPT to simulate advection-diffusion mass transport in the void space of the generated packings, and estimate the asymptotic values of the corresponding hydrodynamic dispersion coefficients. Ease of parallelization of LBM and RWPT program codes enabled efficient use of supercomputing facilities, which allowed to perform resolution studies up to a value of $n = 90$ lattice nodes per sphere diameter and to observe grid independence of the simulated dispersion coefficients (with respect to highest employed resolution). Most simulations were performed at $n = 60$, which decreased the relative (to $n = 90$) error in the simulated dispersion coefficients resulting from the discrete grid to about 10^{-2} .

The porosity-scaling of the dispersion coefficient depends on the packing type: for example, the dispersion coefficient of Rx0.001 packings increases steeply with the bed porosity, while the dispersion coefficient of Ω x0.95 packings is generally low and virtually independent of the bed porosity. Our simulations have revealed that in bulk, monodisperse, random sphere packings between the random-close and random-loose packing limit ($\varepsilon = 0.366-0.46$) variations in the DoH of the packings may lead to a difference in dispersion coefficients up to factor of 2.5. The systematic variation of packing microstructures yielded a comprehensive set of dispersion coefficients, which allowed us to demonstrate good-to-excellent agreement with experimental and simulated dispersion data available in the literature.

Acknowledgments

This work was supported by the Deutsche Forschungsgemeinschaft DFG (Bonn, Germany) under grants TA 268/4-1 and TA 268/5-1. Computational resources on an IBM BlueGene[®]/P platform were provided by JUGENE at Forschungszentrum Jülich, Germany. We are grateful to the John von Neumann Institute for Computing (NIC) and the Jülich Supercomputing Centre (JSC) for allocation of a special CPU-time grant (NIC project number: 4717, JSC project ID: HMR10).

References

- [1] J. Bear, *Dynamics of fluids in porous media*, Dover Publications, 1988.
- [2] F. A. L. Dullien, *Porous media: fluid transport and pore structure*, 2 ed., Academic Press, 1992.
- [3] T. Aste, M. Saadatfar, and T. J. Senden, Geometrical structure of disordered sphere packings, *Phys. Rev. E*, 71 (2005), 061302.
- [4] R. Mizutani, A. Takeuchi, R. Y. Osamura, S. Takekoshi, K. Uesugi and Y. and Suzuki, Submicrometer tomographic resolution examined using a micro-fabricated test object, *Micron*, 41 (2010), 90–95.
- [5] M. Piller, G. Schena, M. Nolich, S. Favretto, F. Radaelli and E. Rossi, Analysis of hydraulic permeability in porous media: from high resolution X-ray tomography to direct numerical simulation, *Transp. Porous Media*, 80 (2009), 57–78.
- [6] B. Manz, L. F. Gladden and P. B. Warren, Flow and dispersion in porous media: lattice-Boltzmann and NMR studies, *AIChE J.*, 45 (1999), 1845–1854.
- [7] S. Bruns, T. Müllner, M. Kollmann, J. Schachtner, A. Höltzel and U. Tallarek, Confocal laser scanning microscopy method for quantitative characterization of silica monolith morphology, *Anal. Chem.*, 82 (2010), 6569–6575.
- [8] S. Bruns and U. Tallarek, Physical reconstruction of packed beds and their morphological analysis: core-shell packings as an example, *J. Chromatogr. A*, 1218 (2011), 1849–1860.
- [9] S. Khirevich, A. Daneyko, A. Höltzel, A. Seidel-Morgenstern and U. Tallarek, Statistical analysis of packed beds, the origin of short-range disorder, and its impact on eddy dispersion, *J. Chromatogr. A*, 1217 (2010), 4713–4722.
- [10] S. Khirevich, A. Höltzel, A. Daneyko, A. Seidel-Morgenstern and U. Tallarek, Structure–transport correlation for the diffusive tortuosity of bulk, monodisperse, random sphere packings, *J. Chromatogr. A*, 1218 (2011), 6489–6497.
- [11] A. Daneyko, A. Höltzel, S. Khirevich and U. Tallarek, Influence of the particle size distribution on hydraulic permeability and eddy dispersion in bulk packings, *Anal. Chem.*, 83 (2011), 3903–3910.
- [12] J. C. Giddings, ‘Eddy’ diffusion in chromatography, *Nature*, 184 (1959), 357–358.
- [13] I. Schenker, F. T. Filser, L.J. Gauckler, T. Aste and H. J. Herrmann, Quantification of the heterogeneity of particle packings, *Phys. Rev. E*, 80 (2009), 021302.
- [14] W. S. Jodrey and E. M. Tory, E. M., Computer simulation of close random packing of equal spheres, *Phys. Rev. A*, 32 (1985), 2347–2351.
- [15] M. P. Allen and D. J. Tildesley, *Computer simulation of liquids*, Oxford University Press, 1989.
- [16] A. Z. Zinchenko, Algorithm for random close packing of spheres with periodic boundary conditions, *J. Comput. Phys.*, 114 (1994), 298–307.
- [17] A. Okabe, B. Boots, K. Sugihara and S. N. Chiu, *Spatial tessellations: concepts and applications of Voronoi diagrams*, 2 ed., John Wiley & Sons, 2000.
- [18] S. Succi, *The lattice Boltzmann equation for fluid dynamics and beyond*, Oxford University Press, 2001.
- [19] C. Pan, L.-S. Luo, and C. T. Miller, An evaluation of lattice Boltzmann schemes for porous medium flow simulation, *Comput. Fluids*, 35 (2006), 898–909.
- [20] I. Ginzbourg and P. M. Adler, Boundary flow condition analysis for the three-dimensional lattice Boltzmann model, *J. Phys. II*, 4 (1994), 191–214.
- [21] Z. Guo, C. Zheng and B. Shi, Discrete lattice effects on the forcing term in the lattice Boltz-

- mann method, *Phys. Rev. E*, 65 (2002), 046308.
- [22] A. N. Tikhonov and A. A. Samarskii, *Equations of mathematical physics*, Dover Publications, 1990.
- [23] O. C. Zienkiewicz, P. Nithiarasu and R. L. Taylor, *The finite element method for fluid dynamics*, Elsevier Butterworth-Heinemann, 2005.
- [24] B. H. Devkota and J. Imberger, Lagrangian modeling of advection-diffusion transport in open channel flow, *Water Resour. Res.*, 45 (2009), W12406.
- [25] B. Lin and R. A. Falconer, Tidal flow and transport modeling using ULTIMATE QUICKEST scheme, *J. Hydraul. Eng.*, 123 (1997), 303-314.
- [26] B. P. Leonard, The ULTIMATE conservative difference scheme applied to unsteady one-dimensional advection, *Comput. Methods Appl. Mech. Eng.*, 88 (1991), 17-74.
- [27] A. E. Hassan and M. M. Mohamed, On using particle tracking methods to simulate transport in single-continuum and dual continua porous media, *J. Hydrol.*, 275 (2003), 242-260.
- [28] S. Khirevich, A. Höltzel, A. Seidel-Morgenstern and U. Tallarek, Time and length scales of eddy dispersion in chromatographic beds, *Anal. Chem.*, 81 (2009), 7057-7066.
- [29] P. Salamon, D. Fernández-García and J. J. Gómez-Hernández, Modeling tracer transport at the MADE site: the importance of heterogeneity, *Water Resour. Res.*, 43 (2007), W08404.
- [30] J. A. Rudnick and G. D. Gaspari, *Elements of the random walk: an introduction for advanced students and researchers*, Cambridge University Press, 2004.
- [31] F. Delay, P. Ackerer and C. Danquigny, Simulating solute transport in porous or fractured formations using random walk particle tracking: a review, *Vadose Zone J.*, 4 (2005), 360-379.
- [32] P. Salamon, D. Fernández-García and J. J. Gómez-Hernández, J. J., A review and numerical assessment of the random walk particle tracking method, *J. Contam. Hydrol.*, 87 (2006), 277-305.
- [33] R. S. Maier, D. M. Kroll, R. S. Bernard, S. E. Howington, J. F. Peters and H. T. Davis, Pore-scale simulation of dispersion, *Phys. Fluids*, 12 (2000), 2065-2079.
- [34] H. Freund, J. Bauer, T. Zeiser and G. Emig, Detailed simulation of transport processes in fixed-beds, *Ind. Eng. Chem. Res.*, 44 (2005), 6423-6434.
- [35] P. E. Kloeden and E. Platen, *Numerical solution of stochastic differential equations*, Springer-Verlag, 1995.
- [36] P. Szymczak and A. J. C. Ladd, Boundary conditions for stochastic solutions of the convection-diffusion equation, *Phys. Rev. E*, 68 (2003), 036704.
- [37] P. H. Israelsson, Y. D. Kim and E. E. Adams, A comparison of three Lagrangian approaches for extending near field mixing calculations, *Environ. Modell. Software*, 21 (2006), 1631-1649.
- [38] S. Khirevich, High-performance computing of flow, diffusion, and hydrodynamic dispersion in random sphere packings, PhD thesis, Philipps University of Marburg, Germany, 2010.
- [39] S. Khirevich, A. Daneyko and U. Tallarek, Simulation of fluid flow and mass transport at extreme scale, Technical Report FZJ-JSC-IB-2010-03, Forschungszentrum Jülich, Jülich Supercomputing Centre, 2010.
- [40] H. Brenner, Dispersion resulting from flow through spatially periodic porous media, *Philos. Trans. R. Soc. A*, 297 (1980), 81-133.
- [41] D. Hlushkou and U. Tallarek, Transition from creeping via viscous-inertial to turbulent flow in fixed beds, *J. Chromatogr. A*, 1126 (2006), 70-85.
- [42] J. C. Giddings, *Dynamics of chromatography: principles and theory*, Marcel Dekker, 1965.
- [43] M. R. Schure, R. S. Maier, D. M. Kroll and H. T. Davis, Simulation of packed-bed chromatog-

- raphy utilizing high-resolution flow fields: comparison with models, *Anal. Chem.*, 74 (2002), 6006–6016.
- [44] G. Taylor, Dispersion of soluble matter in solvent flowing slowly through a tube, *Philos. Trans. R. Soc. A*, 219 (1953), 186–203.
- [45] R. Aris, On the dispersion of a solute in a fluid flowing through a tube, *Philos. Trans. R. Soc. A*, 235 (1956), 67–77.
- [46] D. Dutta, A. Ramachandran and D. T. Leighton, Effect of channel geometry on solute dispersion in pressure-driven microfluidic systems, *Microfluid. Nanofluid.*, 2 (2006), 275–290.
- [47] C. P. Lowe and D. Frenkel, Do hydrodynamic dispersion coefficients exist?, *Phys. Rev. Lett.*, 77 (1996), 4552–4555.
- [48] R. S. Maier and R. S. Bernard, Lattice-Boltzmann accuracy in pore-scale flow simulation, *J. Comput. Phys.*, 229 (2010), 233–255.
- [49] D. L. Koch, R. J. Hill and A. S. Sangani, Brinkman screening and the covariance of the fluid velocity in fixed beds, *Phys. Fluids*, 10 (1998), 3035–3037.
- [50] D. Frenkel and M. H. Ernst, Simulation of diffusion in a two-dimensional lattice-gas cellular automaton: a test of mode-coupling theory, *Phys. Rev. Lett.*, 63 (1989), 2165–2168.
- [51] R. H. M. Merks, A. G. Hoekstra and P. M. A. Sloot, The moment propagation method for advection–diffusion in the lattice Boltzmann method: validation and Péclet number limits, *J. Comput. Phys.*, 183 (2002), 563–576.
- [52] R. S. Maier, M. R. Schure, J. P. Gage and J. D. Seymour, Sensitivity of pore-scale dispersion to the construction of random bead packs, *Water Resour. Res.*, 44 (2008), W06S03.
- [53] J. D. Seymour and P. T. Callaghan, Generalized approach to NMR analysis of flow and dispersion in porous media, *AIChE J.*, 43 (1997), 2096–2111.
- [54] F. Augier, F. Idoux and J. Y. Delenne, Numerical simulations of transfer and transport properties inside packed beds of spherical particles, *Chem. Eng. Sci.*, 65 (2010), 1055–1064.
- [55] U. M. Scheven, R. Harris and M. L. Johns, Intrinsic dispersivity of randomly packed monodisperse spheres, *Phys. Rev. Lett.*, 99 (2007), 054502.
- [56] M. Sahimi, *Flow and transport in porous media and fractured rock: from classical methods to modern approaches*, Wiley-VCH, 1995.
- [57] R. S. Maier, D. M. Kroll and H. T. Davis, Diameter-dependent dispersion in packed cylinders, *AIChE J.*, 53 (2007), 527–530.
- [58] P. A. Cundall and O. D. L. Strack, A discrete numerical model for granular assemblies, *Geotechnique*, 29 (1979), 47–65.
- [59] U. M. Scheven, Dispersion in non-ideal packed beds, *AIChE J.*, 56 (2010), 289–297.
- [60] P. G. Saffman, A theory of dispersion in a porous medium, *J. Fluid Mech.*, 6 (1959), 321–349.
- [61] P. G. Saffman, Dispersion due to molecular diffusion and macroscopic mixing in flow through a network of capillaries, *J. Fluid Mech.*, 7 (1960), 194–208.
- [62] S. P. Kuttanikkad, Pore-scale direct numerical simulation of flow and transport in porous media, PhD thesis, Ruprecht Karls University of Heidelberg, Germany, 2009.